Energy dependence of the complex symmetry term in the empirical nucleon-nucleus optical model potential

J.P. Delaroche, E. Bauge, P. Romain, S. Vuillier*

Service de Physique Nucléaire
Centre d'Études de Bruyères-le-Châtel
BP 12, 91680 Bruyères-le-Châtel, France

Abstract

A joint optical model analysis of proton and neutron scattering and reaction cross sections is performed up to 200 MeV for ^{54,56}Fe, ^{58,60}Ni, ^{181}Ta, ^{182,184,186}W and ^{208}Pb. The energy dependent optical model potentials (OMPs) deduced with or without including dispersion relations are used to build the symmetry component of the OMPs, separately for each target nucleus. It is found that the symmetry potentials are complex and display sharp energy dependences. Volume integrals are deduced and compared with JLM model predictions and properties of the Love and Franey t-matrix.

1 Introduction

Elastic scattering of protons and neutrons in a narrow energy range, typically 10 - 40 MeV, has been the tool for investigating the nucleon-nucleus optical model potential (OMP) properties. The empirical neutron and proton OMPs display differences which are explained in terms of Coulomb correction (ΔU_C) and isovector (U_1) potentials. This information on the OMP components is limited because (i) linear energy dependences are usually assumed for the potential depths, and (ii) the effective mass is ignored when determining ΔU_C and U_1 [1]. For these reasons, extrapolating ΔU_C and U_1 to higher incident energies is questionable.

In this work, we follow the method of [1] to determine the isovector potentials for several nuclei (^{54,56}Fe, ^{58,60}Ni, ^{181}Ta, ^{182,184,186}W, ^{208}Pb) over a broad energy range ($E \leq 200$ MeV). Our goal is not the derivation of U_1 global properties, but rather a mapping of shape and depth evolutions of these OMP components with increasing mass and energy.

The database considered in these empirical OMP analyses includes all existing measurements for differential cross sections, analyzing powers, reaction and total cross sections. The OMP calculations for Fe and Ni isotopes are performed without including dispersion relations. Dispersive OMP analyses are shown for the heavier nuclei. ^{208}Pb is considered as a spherical nucleus, while the deformed nuclei ^{181}Ta and ^{182,184,186}W are treated in the coupled channels framework [2].

2 Isovector potential

Detailed discussions on how isovector potentials should be extracted from proton and neutron OMPs are presented in [1]. We follow this method to establish our notations, separately for the real and imaginary components.

2.1 Real component

In asymmetric nuclear matter, the real potential felt by neutrons and protons is [1]

$$V_n(E) = V_0(E - \alpha V_1) + \alpha V_1$$

and

$$V_p(E) = V_0(E - V_C + \alpha V_1) - \alpha V_1,$$

respectively. In these expressions, E is the incident energy, V_C the Coulomb potential, and $\alpha = (N-Z)/A$ the asymmetry parameter. Expanding $V_n(E + \alpha V_1)$ and $V_p(E - \alpha V_1 + V_C)$ up to first order yields

$$V_1(E) = [2\alpha \frac{m^*}{m}(E)]^{-1}[V_n(E) - V_p(E + V_C)], \tag{1}$$

with

$$\frac{m^*}{m}(E) = 1 - \frac{1}{2}\frac{\partial}{\partial E}(V_n(E) + V_p(E + V_C)).$$

For spherical nuclei, the isovector term $V_1(r, E)$ is deduced by analogy with eq.(1)

$$V_1(r, E) = [2\alpha \frac{m^*}{m}(r, E)]^{-1}[V_n(r, E) - V_p(r, E + \bar{V}_C)], \tag{2}$$

where

$$\frac{m^*}{m}(r, E) = 1 - \frac{1}{2}\frac{\partial}{\partial E}(V_n(r, E) + V_p(r, E + \bar{V}_C)),$$

and $\bar{V}_C$ is the Coulomb potential averaged over radial coordinates.

For axially deformed nuclei, the isovector potential in the body-fixed system of coordinates is labeled $V_1(\overrightarrow{r}, E)$. It is defined, like in eq.(2), in terms of the deformed neutron and proton OMPs $V_n(\overrightarrow{r}, E)$ and $V_p(\overrightarrow{r}, E + \bar{V}_C)$ and their first derivatives with respect to energy. The radial shape of $V_1(\overrightarrow{r}, E)$ is obtained through a multipole expansion

$$V_1(\overrightarrow{r}, E) = \sum_{\substack{\lambda \geq 0 \\ and\ even}} V_{1,\lambda}(r, E)Y_\lambda(\Omega'). \tag{3}$$

where the angle Ω' refers to the body-fixed system.

2.2 Imaginary component

This potential component is labeled W_1. Its derivation follows that adopted for V_1. For instance,

$$W_1(r, E) = [2\alpha \frac{\tilde{m}^*}{m}(r, E)]^{-1}[W_n(r, E) - W_p(r, E + \bar{V}_C)], \tag{4}$$

with

$$\frac{\tilde{m}^*}{m}(r, E) = 1 - \frac{1}{2}\frac{\partial}{\partial E}(W_n(r, E) + W_p(r, E + \bar{V}_C)),$$

and with W_n and W_p as the neutron and proton imaginary OMPs for spherical nuclei, respectively.

3 Neutron and proton OMPs

3.1 Nucleon + ^{54,56}Fe and nucleon + ^{58,60}Ni systems

The Fe and Ni isotopes are treated as spherical nuclei, and the nucleon-nucleus OMP adopted here has the familiar form

$$U_q(r, E) = -V_q(r, E) - iW_q(r, E) + V_C(r)$$

$$+\lambdabar_\pi^2(V_{q,SO}(r, E) + iW_{q,SO}(r, E))\overrightarrow{l}.\overrightarrow{s}, \tag{5}$$

where the symbol q stands for proton or neutron ($q = p,n$). V_C is the Coulomb potential of a uniform charge distribution ($q = p$, only), $V_q(r, E) = V_q(E)f_{q,V}(r)$, $W_q(r, E) = W_{q,V}(E)f_{q,W}(r) - 4a_D W_{q,D}(E)$

$\times \frac{d}{dr} f_{q,D}(r)$, $V_{q,SO}(r, E) = V_{q,SO}(E) \lambda_\pi^2 \times \frac{1}{r} \frac{d}{dr} f_{q,SO}(r)$, and $W_{q,SO}(r, E) = W_{q,SO}(E) \lambda_\pi^2 \frac{1}{r} \frac{d}{dr} f_{q,SO}(r)$, and $f_{q,i}(r)$ a Woods-Saxon shape.

The E-dependent potential depths are parameterized as follows:

$$V_q(E) = V_{0,q} e^{-\lambda_q E},$$

$$W_{q,D}(E) = \frac{a_q (E - \epsilon_{F,q})^n e^{-b_q(E-\epsilon_{F,q})}}{(E - \epsilon_{F,q})^n + c_q^n},$$

$$W_{q,V}(E) = \frac{\alpha_q (E - \bar{\epsilon}_{F,q})^n}{(E - \bar{\epsilon}_{F,q})^n + \beta_q^n}, \tag{6}$$

$$V_{n,SO}(E) = V_{p,SO}(E) = V_{SO}(0) e^{-\mu E},$$

$$W_{n,SO}(E) = W_{p,SO}(E) == W_{SO}(0) - \nu E.$$

With the closed forms adopted in eq.(6), all the potential components display smooth variations with increasing energy. The form taken for the real central potentials is intended to mimic that of volume integrals of potentials in which dispersive terms are included. The forms taken for the imaginary surface and volume components is of common use. Here we adopt the power $n = 4$. The Fermi energies are labeled ϵ_F, and their average over mass and isospin is $\bar{\epsilon}_F$. Since the proton and neutron volume absorptive potentials are found to display similar values in our OMP analyses, the following constraint is imposed

$$W_{n,V}(E) = W_{p,V}(E + \bar{V}_C),$$

where $\bar{V}_C$ is the average Coulomb potential (see Sec.2) determined from charge distributions measured in electron scattering experiments. Relativistic kinematics is used throughout this analysis and that discussed below.

3.2   Nucleon + ^{208}Pb system

Dispersive OM potentials are established in our work. The present analyses represent extensions of those performed earlier [3, 4]. Except for the real central potentials, the closed forms in eq.(6) are adopted. The real central potentials contain two terms. The first one varies smoothly with energy; this is the so-called Hartree-Fock term. The second component is the dispersive term. It includes corrections stemming from the nonlocality of the surface absorption treated in the Perey-Buck approximation [5]. This analysis closely follows that adopted in [2].

3.3   Nucleon + ^{181}Ta system

The dispersive OMPs deduced from coupled channels analyses are presented in [2].

4   Results

In this Section, we first present results from our OMP analysis of neutron and proton scattering and reaction measurements. All the calculations are performed using the code ECIS95 [6]. We then show radial shapes and volume integrals deduced for the isoscalar and isovector potentials.

4.1   Scattering and reaction

The nucleon-nucleus OMP analyses for ^{181}Ta and ^{182,184,186}W are presented in a separate contribution [2]. The agreement between predictions and data is excellent.

In Fig.1 is shown a comparison between differential cross section and analyzing power measurements for protons and neutrons incident on ^{56}Fe, up to 180 MeV. As can be seen, there is a good overall
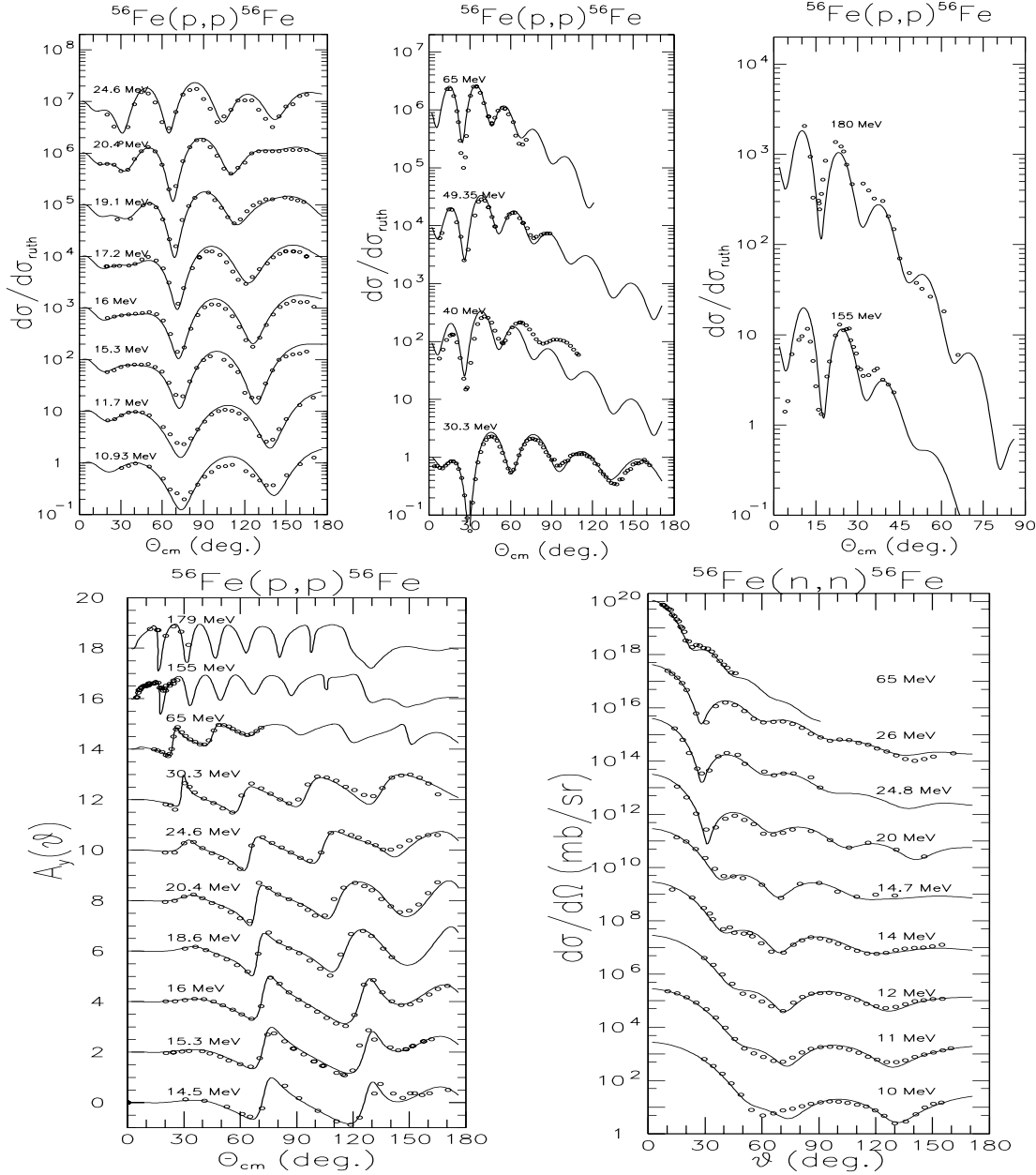

Figure 1: Comparisons between calculated differential cross-sections and analyzing powers, and measurements for protons (neutrons) incident on ^{56}Fe between 10.93 MeV and 180 MeV (10 and 65 MeV). Note that the differential cross-sections above those at 30.3,155 and 10 MeV are offset by factors of 10^2 (and by factor 10, above those at 10.93 MeV), and that analyzing powers above 14.5 MeV are shifted by offsets of 2.

agreement between the experimental data and our OMP predictions. For the total neutron cross sections for elemental iron, the agreement (not shown) is not as good as it is for angular distributions. This is partly due to ignoring the dispersion relations (DR) in our OMP calculations. Including the DR terms in the analyses would lead to improvements in the σ_T predictions for $E \geq 20$ MeV [2]. Below 5 MeV, it is difficult to get a good fit to the σ_T data. This is not surprising since previous OMP studies so far conducted for Fe and Ni isotopes have all met with similar problems at low incident neutron energies. The comparison between angular distribution measurements and OMP predictions has been extended to ^{54}Fe and ^{58,60}Ni. The agreement (not shown) which is obtained in this comparison is as good as it is for ^{56}Fe.
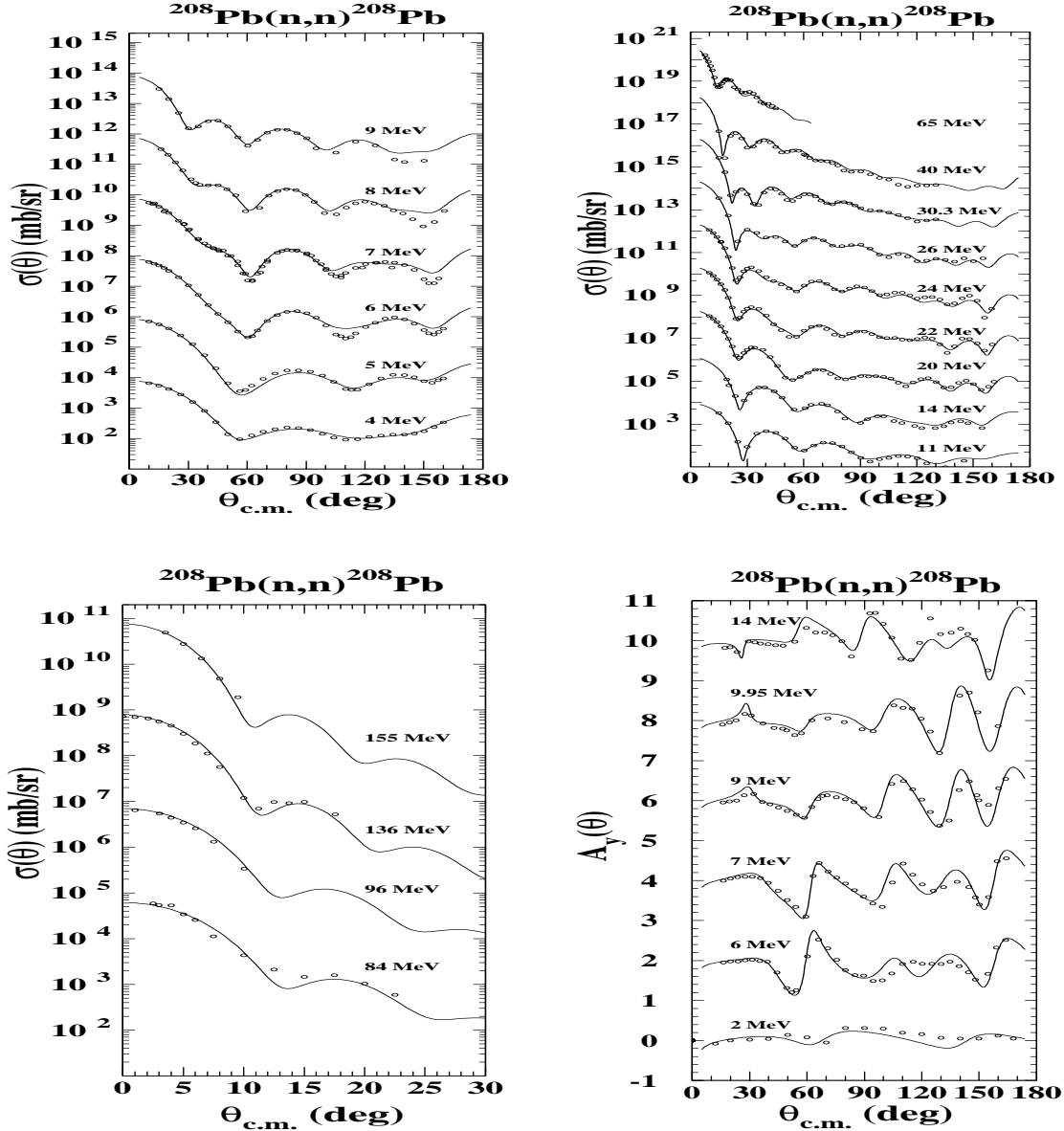

Figure 2: Comparisons between calculated differential cross-sections and analyzing powers, and measurements for neutrons incident on ^{208}Pb between 4 MeV and 155 MeV. Note that the differential cross-sections above those at 4,11, and 84 MeV are offset by factors of 10^2, and that analyzing powers above 2 MeV are shifted by offsets of 2.

We now comment on our dispersive OMP analyses conducted for proton and neutron scattering from ^{208}Pb up to 185 MeV. The DR terms are corrected for non-locality of the surface absorption in a manner similar to that explained in [2]. A comparison between measured angular distributions for (p,p) and (n,n) scattering and our dispersive OMP predictions are shown in Figs.2 and 3, respectively. Here also, the agreements obtained in these comparisons are of good quality. The same comments apply to the comparison between σ_T and σ_R data for neutron and proton, respectively, and present OMP calculations (see Fig.4).
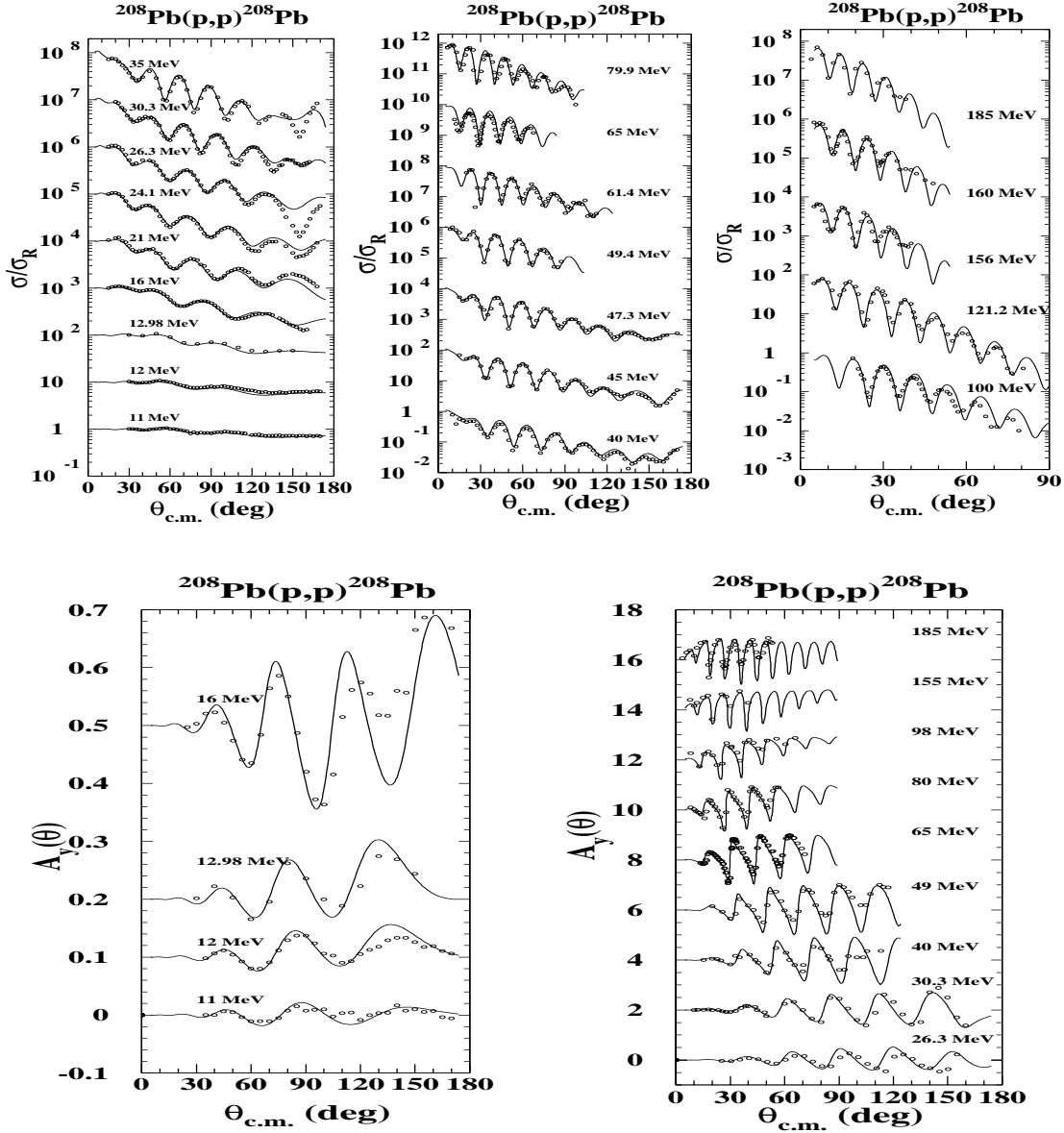

Figure 3: Comparisons between calculated differential cross-sections and analyzing powers, and measurements for protons incident on ^{208}Pb between 11 MeV and 185 MeV. Note that the differential cross-sections above those at 40 and 100 MeV are offset by factors of 10^2 (and by factor 10, above those at 11 MeV), and that analyzing powers above 11,12.98 and 26.3 MeV are shifted by offsets of 0.1,0.5, and 2, respectively.
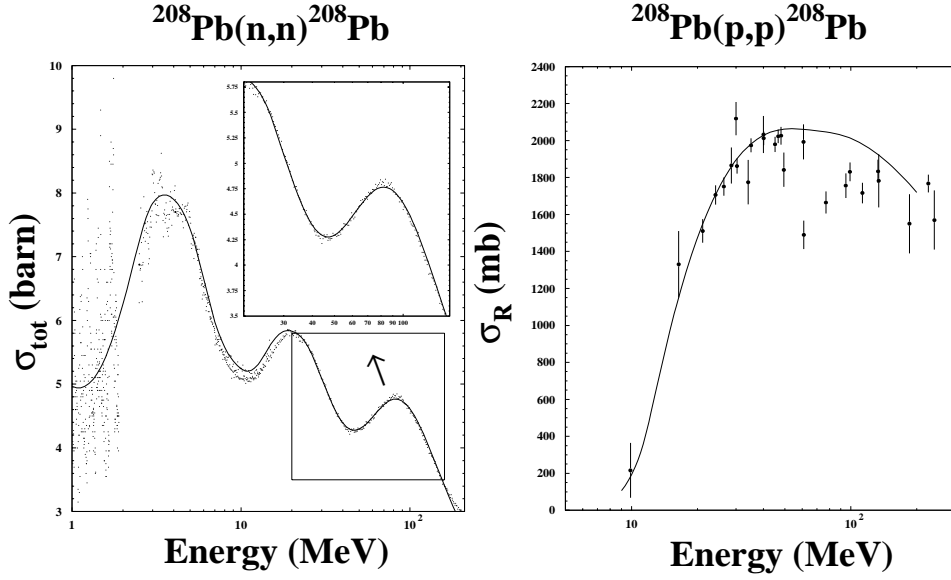
6

Figure 4: Comparisons between present predictions for neutron total cross section and proton reaction cross section and measurements up to 200 MeV for ^{208}Pb.

4.2 Isoscalar and Isovector potentials

The complex isovector potentials are now extracted from our neutron and proton OMPs, following the method outlined in Sec.2. This is performed separately for ^{56}Fe, ^{181}Ta, and ^{208}Pb.
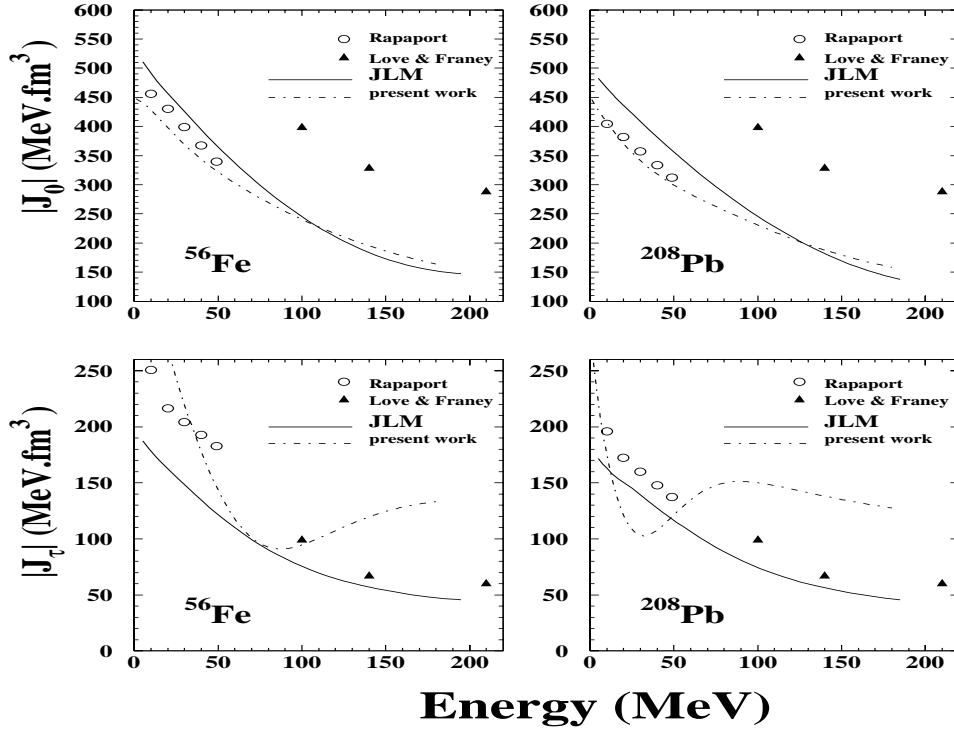

Figure 5: Modulus of the isoscalar and isovector components of the OMP for ^{56}Fe and ^{208}Pb.

Here we present results only for ^{56}Fe and ^{208}Pb. The modulus of the volume integrals for the isoscalar ($|J_0|$) and isovector ($|J_\tau|$) potentials are shown in Fig.5. The dashed curves are from our phenomenological OMP analyses, and the continuous curves from present JLM model calculations. The circles are deduced from the global potential of Rapaport et al. [7] and the triangles are taken from the work [8] of Love and Franey (LF). For $|J_0|$ (see top panels), a good agreement between the analyses is obtained except for the LF predictions which are far too apart. On the other hand, the JLM and LF predictions are in reasonable agreement for $|J_\tau|$ (see bottom panels). In contrast, our phenomenological OMP results show significant deviations from the other three calculations.

4.3 Radial shapes

In Fig.6 are shown the radial shapes deduced from the present phenomenological OMP analyses for ^{208}Pb. This figure includes both complex isoscalar (see top panels) and isovector components (see bottom panels). As can be seen, the isovector potentials are strongly E-dependent, and their radial shapes are superpositions of surface and volume terms.
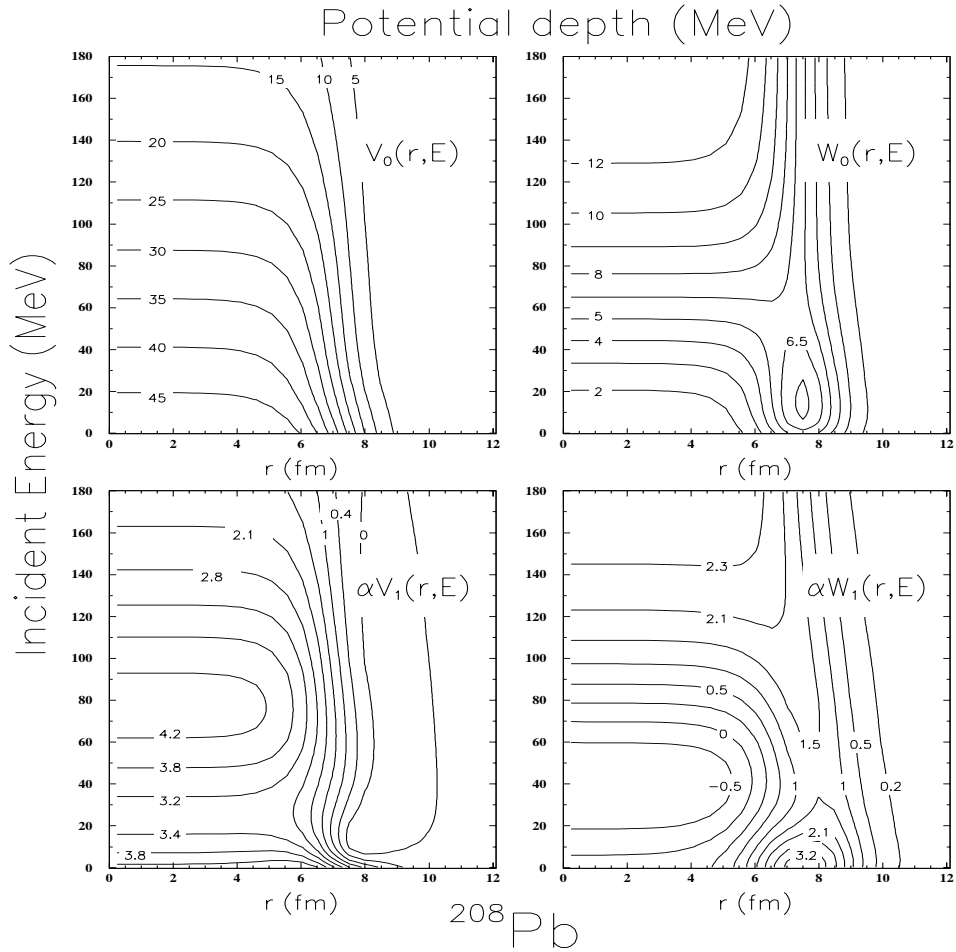

Figure 6: ^{208}Pb. Radial shapes and energy dependences of the isoscalar and isovector OMP components.

5   Conclusion

In the present work we have analyzed nucleon scattering measurements up to 200 MeV for several nuclei with masses A = 54 - 208 following a method suggested by Mahaux and Sartor. Isoscalar and isovector complex potentials are deduced which display intricate E-dependences. Obviously these predictions need to be challenged through comparisons to $\Delta S = 0$ (p,n) cross sections.

(*) Now at Laboratoire National Saturne, Saclay, France

References

[1] C.Mahaux and R.Sartor, Nucl. Phys. **A481**, 407 (1988)

[2] P.Romain and J.P.Delaroche, contribution to this Workshop

[3] C.H.Johnson, D.J.Horen and C.Mahaux, Phys. Rev C **36**, 2252 (1987)

[4] R.W.Finlay *et al.*, Phys. Rev. C **39**, 804 (1989)

[5] F.Perey and B.Buck, Nucl. Phys. **32**, 353 (1962)

[6] J.Raynal, code ECIS95, unpublished.

[7] J.Rapaport, in The (p,n) Reaction and the Nucleon-Nucleon Force (Plenum,NY,1980), p.233

[8] W.G.Love and M.A.Franey, Phys. Rev. C **24**, 1073 (1981)